PAPER

SiO2 assisted Cu0–Cu+–NH2 composite interfaces for efficient CO2 electroreduction to C2+ products†

Zi-Yang Zhang,‡[a] Hao Tian,‡[a] Han Jiao,[a] Xin Wang,[a] Lei Bian,[a] Yuan Liu, [ID] [a] Nithima Khaorapapong, [ID] [b] Yusuke Yamauchi [ID] [cde] and Zhong-Li Wang [ID] *[a]

The electrochemical CO_2 reduction reaction (CO_2RR) for high value-added multi-carbon product (C_{2+}) production over copper oxide-based catalysts is an important way to realize the carbon cycle. However, developing effective reaction interfaces and microenvironments to improve the Faraday efficiency (FE) and current density of C_{2+} remains a major challenge. Herein, we construct Cu^0–Cu^+–NH_2 composite interfaces with the assistance of SiO_2. Using Cu_2O nanoparticles as a model catalyst, a layer of porous SiO_2 is first coated on the surface of the particles, and then, a silane coupling agent containing $-NH_2$ is bonded on the surface of SiO_2. The strong interaction between SiO_2 and Cu_2O at the interface induces the oxidation effect of low valent Cu, and even under the CO_2RR, part of Cu^+ is reduced to Cu^0 and part of Cu^+ still maintains positive valence, forming the interface of Cu^0–Cu^+. SiO_2 also acts as a bridge between copper species and $-NH_2$ to create a Cu catalyst–NH_2 group interface. With the help of the synergistic effect of the composite interfaces, the optimized $Cu_2O@SiO_2$–NH_2 catalyst achieves a FE of 81.2% for C_{2+} products with a current density of 292 mA cm^{-2} at −1.7 V *versus* a reversible hydrogen electrode. *In situ* Raman and attenuate total reflectance-infrared absorption spectroscopy spectra show that the interaction between surface $-NH_2$ and CO_2 molecules enhances the adsorption and activation process of CO_2 and promotes the formation of CO intermediates (*CO). On the Cu^0–Cu^+ interface, the C–C coupling process between *CO is accelerated, and the two interfaces synergistically promote the generation of C_{2+} products. This work provides a new strategy for constructing composite interfaces to improve the CO_2RR to C_{2+} products.

1. Introduction

The excessive emission of CO_2 breaks the balance of the natural carbon cycle;[1] therefore, it is urgent to develop new technologies for CO_2 recycling and utilization to realize the sustainable development of resources and energy, and mitigate global warming. The electrochemical CO_2 reduction reaction (CO_2RR) coupled with renewable electric energy can not only synthesize high-value-added products from CO_2 but also realize energy storage at the same time, which is a promising way of CO_2 utilization.[2,3] Up to now, it has been reported that at least 16 distinct products are formed from the CO_2RR, such as CO, CH_4, HCOOH, C_2H_4, C_2H_5OH, C_3H_7OH, and so on.[4,5] Among the CO_2RR products, C_{2+} can be used as a chemical raw material and fuel, leading to wide application.[1,6] Consequently, researchers have made significant endeavors in the synthesis of C_{2+} through the CO_2RR. However, CO_2 is a linear and inert molecule with a C=O bond energy of up to 750 kJ mol^{-1}.[7] Thus, achieving C=O activation under milder conditions requires the use of appropriate catalysts. Currently reported catalysts for CO_2RR synthesis of C_{2+} products are mainly Cu-based catalysts, because they have a moderate adsorption strength for C_1 intermediates in the CO_2RR process, which is neither too strong for desorption nor too weak for further adsorption activation for subsequent reactions, to promote the dimerization between C_1 intermediates and generate C_{2+} products.[1,8]

Among Cu-based catalysts, the oxides of Cu and their derivatives are an important type of catalyst with high reactivity.[9–11] During the reduction and reconstruction process, abundant metal-oxide (Cu^0–$Cu^{\delta+}$) interfaces are generated for Cu oxides, which significantly enhance the activity of the catalysts and improve the rate of C–C coupling.[12] Therefore, their

[a]Tianjin Key Laboratory of Applied Catalysis Science & Technology, School of Chemical Engineering and Technology, Tianjin University, Tianjin 300072, China. E-mail: wang. zhongli@tju.edu.cn

[b]Materials Chemistry Research Center, Department of Chemistry and Center of Excellence for Innovation in Chemistry, Faculty of Science, Khon Kaen University, Khon Kaen 40002, Thailand

[c]Australian Institute for Bioengineering and Nanotechnology (AIBN), The University of Queensland, Brisbane, QLD 4072, Australia

[d]Department of Materials Process Engineering, Graduate School of Engineering, Nagoya University, Nagoya, 464–8603 Japan

[e]Department of Chemical and Biomolecular Engineering, Yonsei University, 50 Yonsei-ro, Seodaemun-gu, Seoul, 03722 South Korea

† Electronic supplementary information (ESI) available. See DOI: https://doi.org/10.1039/d3ta05652j

‡ The authors contributed equally to this work.

electronic structure[13] and morphology[14,15] have been widely studied to improve the activity of the CO_2RR to C_{2+} products. Especially, recent studies have found that the adsorption strength of the CO intermediate (*CO) on $Cu^{\delta+}$ species ($0 < \delta < 2$) is stronger than that on Cu^0 species at the metal-oxide interface,[16–18] which is beneficial to increase the concentration of *CO on the catalyst surface and promote the *CO dimerization step. Therefore, it is important to improve the stability of $Cu^{\delta+}$ species under reduction conditions to produce C_{2+} products. For example, Zhou et al.[16] reported a B-doped Cu catalyst to regulate the local electronic structure of Cu and improve the stability of positive valence Cu. Consequently, the adsorption and dimerization of *CO can be controlled by adjusting the average oxidation valence of Cu, which makes the Cu(B) catalyst achieve 79% faradaic efficiency (FE) of C_2 in the CO_2RR process. In addition, Yan et al.[19] reported a hexagonal boron nitride (h-BN) modified Cu_2O catalyst, where the strong electron interaction between the two components of Cu_2O and BN makes the electrons on Cu_2O transfer to BN to strengthen the Cu–O bond, thus stabilizing the Cu^+ species during the CO_2RR. Upon applying the Cu_2O-BN catalyst for the CO_2RR process, the ratio of C_2H_4/CO increased by 1.62 times compared with that of the Cu_2O catalyst. Similarly, Zang et al.[20] designed a carbon-coated CuO_x (CuO_x@C) catalyst and the carbon layer on the catalyst surface effectively stabilized Cu^+ species, thereby facilitating the C–C coupling process. In the CO_2RR process, the FE of ethanol reached 46%, and the partial current density reached 166 mA cm^{-2}. A series of studies have proven that the interfaces between Cu^+ and Cu^0 regions could promote C_{2+} production. Additionally, organic molecules containing amino groups (–NH_2) are often used as surface modifiers to regulate the surface properties of catalysts, thereby altering the reaction microenvironment during the CO_2RR. Li et al.[21] constructed a molecular–catalyst interface by modifying a layer of an N-aryl-dihydropyridine-based oligomer on the surface of the Cu catalyst, which made the catalyst exhibit excellent ethylene selectivity with an FE of 72% at −0.83 V versus the reversible hydrogen electrode (vs. RHE; the same potential scale is used in the following discussion unless otherwise specified) during the CO_2RR. Similarly, Chen et al.[22] incorporated polyamine on Cu electrodes. Due to the strong binding force between the CO_2/CO molecule and –NH_2, the polyamine–Cu interface formed a microenvironment with locally high concentrations of CO_2 and CO, which accelerates the formation of ethylene and the FE reached 72% at −0.97 V. According to the above discussion, the Cu^0–Cu^+ reaction interface and –NH_2 induced molecular–catalyst interface both can promote the formation of C_{2+} products in the CO_2RR.

The widely suggested CO_2-to-C_{2+} conversion mechanisms show that the promoted CO_2 activation, the faster formation and adsorption of the C_1 intermediate, and the accelerated C–C coupling process are essential to increase the selectivity of C_{2+} products. However, developing a reaction interface that simultaneously meets the requirements of three aspects still faces great challenges. In this work, we construct a Cu^0–Cu^+–NH_2 composite reaction interface with the assistance of SiO_2, which includes both the Cu-based Cu^0–Cu^+ interface and the Cu catalyst–NH_2 group interface. We have fully utilized two characteristics of amorphous SiO_2: firstly, it can uniformly coat inorganic nanoparticles, and secondly, it can bond with silane coupling agents to introduce organic functional groups. Using Cu_2O nanoparticles as a model catalyst, a layer of porous SiO_2 is first coated on the surface of the particles (named Cu_2O@SiO_2). Under the conditions of electrochemical reduction, part of Cu^+ is reduced to Cu^0, and part of Cu^+ maintains positive valence under the strong interaction of SiO_2, forming the interface of Cu^0–Cu^+. Then, a silane coupling agent containing –NH_2 is bonded on the surface of SiO_2 (named Cu_2O@SiO_2–NH_2), and the SiO_2 coating acts as a bridge between copper species and –NH_2 to form a Cu catalyst–NH_2 group interface. With the help of the synergistic effect of the Cu^0–Cu^+–NH_2 composite interfaces, the optimized Cu_2O@SiO_2–NH_2 catalyst achieves a selectivity of 81.2% for C_{2+} products at a current density of 292 mA cm^{-2} at −1.7 V (without iR compensation). In situ Raman and attenuate total reflectance-infrared absorption spectroscopy (ATR-IRAS) spectra show that the interaction between surface –NH_2 and CO_2 molecules enhances the adsorption and activation process of CO_2 and promotes the formation of *CO, which increases the local concentration of surface *CO. On the Cu^0–Cu^+ interface, the C–C coupling process between *CO is accelerated, and the two interfaces synergistically promote the generation of C_{2+} products. This work provides a new strategy for constructing composite interfaces to promote the CO_2RR to C_{2+} product conversion under high current density.

2. Experimental section

2.1 Materials

All reagents involved in this study were commercially available and used without further purification: $CuCl_2\cdot2H_2O$ (AR, Jiang-Tian), NaOH (AR, MACKLIN), Na_2CO_3 (AR, JiangTian), KCl (AR, JiangTian), ethyl orthosilicate (GC, Aladdin), aminopropyl triethoxysilane (AR, HEOWNS), ascorbic acid (AR, JiangTian), n-octane (AR, MERYER), L-arginine (AR, JiangTian), polyvinylpyrrolidone (MW = 58 000, MACKLIN). All aqueous solutions were prepared with deionized water. A proton exchange membrane (Nafion 211, DuPont), Nafion (5 wt%, Sigma-Aldrich), isopropanol (>99%, Aladdin), carbon NPs (50 nm, Sigma-Aldrich), and graphite (Aladdin) were obtained.

2.2 Catalyst preparation

Cu_2O dodecahedron nanoparticles were synthesized by a method reported in the literature.[23] 1.11 g PVP was dissolved into deionized water, and then 10 mL of 0.1 mol L^{-1} $CuCl_2\cdot2H_2O$ was also added into the above solution dropwise, under stirring and heating to 55 °C. Then 10 mL of 2 mol L^{-1} NaOH solution was added. After stirring at 55 °C for 30 min, 10 mL of 1 mol L^{-1} ascorbic acid solution was added to the mixture and continued to stir at 55 °C for 3 h. Then, the precipitation was centrifuged and washed in deionized water and anhydrous ethanol 3 times to obtain Cu_2O dodecahedron nanoparticles.

Then the Cu_2O nanoparticles were modified with SiO_2 and –NH_2.[24] 0.73 g n-octane and 0.014 g L-arginine were added into

This journal is © The Royal Society of Chemistry 2024

J. Mater. Chem. A, 2024, **12**, 1218–1232 | **1219**

15 mL deionized water and stirred vigorously at 60 °C. *n*-Octane was used as the solvent to prevent excessive polymerization of SiO_2, and to control the formation process of SiO_2 on the surface of Cu_2O. After that, 25 μL ethyl orthosilicate (TEOS) was added to the mixture and stirred at 60 °C for 4 h. Then 0.2 g Cu_2O dodecahedron nanoparticles were added into the mixture and stirred at room temperature for 20 h. The precipitation was centrifuged and washed three times with deionized water and anhydrous ethanol to obtain $Cu_2O@SiO_2$ nanoparticles. The obtained $Cu_2O@SiO_2$ nanoparticles were evenly dispersed into 25 mL anhydrous ethanol, and then 25 μL aminopropyl trie-thoxysilane (APTES) was added, and stirred at room temperature for 24 h. The precipitation was centrifuged, washed three times with anhydrous ethanol and deionized water, and dried by vacuum at room temperature for 12 h. $Cu_2O@SiO_2–NH_2$ nanoparticles were obtained. For the control sample of $Cu_2O@SiO_2$, the amount of TEOS was increased to 50 μL during the SiO_2 coating process to maintain a coating thickness similar to that of the $Cu_2O@SiO_2–NH_2$ sample.

2.3 Catalyst characterization

Scanning electron microscopy (SEM) images were obtained on a Hitachi S-4800 field emission scanning electron microscopy. Transmission electron microscopy (TEM) and high-angle annular dark-field scanning transmission electron microscopy (HAADF-STEM) were conducted on a JEOL F200 transmission electron microscope with an acceleration voltage of 200 kV. The samples were dispersed in ethanol and ultrasonically treated for 20 min, and then the samples were added dropwise onto a Mo grid ultrathin carbon film. X-ray diffraction was conducted on a Bruker D8 Focus X-ray diffractometer using Cu Kα radiation (λ = 0.15418 nm). The tube voltage and current were 40 kV and 40 mA, respectively. The diffraction angle of samples was recorded from 20° to 80° (2θ) with a scan rate of 5° min^{-1}. N_2 physisorption analysis was conducted at −196 °C using a Tristar 3000 Micromeritics instrument. XPS was conducted on a Thermo-Fisher Scientistic K-Alpha+ instrument. The X-ray radiation source was Al Kα ($h\nu$ = 1486.6 eV) with an X-ray power of 150 W and the spot size was 400 μm. The pass energy was 50 eV. The XPS was calibrated with a C 1s binding energy of 284.8 eV. X-ray absorption fine structure (XAFS) measurements were performed to probe the valence state and the bonding information of Cu species on a TableXAFS-500 X-ray absorption fine structure spectrometer. The CO_2 adsorption experiment was carried out on a BEL SORP-max at 298 K.

2.4 Electrode preparation

We first prepared a conductive gas-diffusion layer by sputtering the Cu layer on a PTFE film, copper target (99.999%). To prepare the catalyst ink, 10 mg of the pre-catalyst and 2 mg of carbon were dispersed in a mixture of 1 mL propanol and 30 μL of 5 wt% Nafion solution (Sigma-Aldrich); 10 mg carbon was dispersed in a mixture of 1 mL of propanol and 50 μL of 5 wt% Nafion solution; 10 mg graphite was dispersed in a mixture of 1 mL of propanol and 70 μL of 5 wt% Nafion solution, and then they were sonicated for at least 1 hour. The ink was airbrushed onto a 2 × 3 cm^2 Cu/PTFE substrate with a loading of ~1 mg cm^{-2}; the carbon–graphite mixture was sprayed on the catalyst surface in turn. The PTFE-based gas diffusion electrode could enhance CO_2 gas mass transfer through hydrophobic PTFE channels and the carbon powder and graphite powder with certain hydrophobicity on the surface of the catalyst could tailor the wettability of the electrolyte and prevent the catalyst from being flooded by aqueous electrolyte. A stainless-steel mesh was used as the anode. Before the reaction, the steel (1.5 × 2 cm^2) was sonicated in acetone and deionized water for 30 min, respectively, and then dried by nitrogen purging for further use.

2.5 Electrochemical CO_2 reduction measurement

The CO_2RR activity of the catalyst was investigated by performing electrolysis in a flow-cell configuration using 1 M KCl as the cathodic and 2 M KOH as the anodic electrolyte. Cl^- anions can specifically adsorb on the inner Helmholtz plane (IHP) of the catalyst surface, which not only confines CO_2 and facilitates electron transfer from the electrode to CO_2 *via* the X_{ad}–C bond but also improves the *CO adsorption for favorable C–C coupling.[25] Moreover, the formation of OH^- during the CO_2RR in the KCl electrolyte leads to a local alkaline environment, and the use of high pH can greatly accelerate the production rates for C_{2+} products.[26] The flow cell consists of a gas diffusion layer as the working electrode (0.5 cm^2), a proton exchange membrane (Nafion 211), a stainless-steel mesh (1500 mesh) as the counter electrode, and Ag/AgCl (saturated KCl) as the reference electrode. An electrochemical workstation (CHI660, Chenhua, Shanghai) was used to perform the CO_2RR test. CO_2 was supplied into gas chambers with a constant rate of 10 mL min^{-1} by using a mass-flow controller, and the outlet gas flow rate was also recorded by the flow controller. The cathodic electrolyte (30 mL) was circulated through the electrolyte chambers under a constant flow (5 mL min^{-1}) *via* a peristaltic pump. The anodic electrolyte was circulated through the anodic chamber by a gas–liquid mixed flow pump. Reactions were tested *via* chronoamperometry for 30 min at different applied potentials from −1.1 V to −1.9 V. Gas products were analyzed *via* online GC (Shimadzu 2010) with a Thermal conductivity detector (TCD) (column: Agilent Carbon Plot (30 m × 0.32 mm × 3 μm)). The FE of gas products was calculated based on the following:

$$\text{FE} = \frac{C_{\text{product}} \times V_{CO_2} \times 10^{-3} \times t \times e \times F}{V_{\text{m}} \times Q} \times 100\%$$

where C_{product} is the concentration of the gas-phase products (mol L^{-1}), ν_{CO_2} is the flow rate of CO_2, t is the reaction time, e is the number of transferred electrons for the product, F the Faraday constant 96 485 C mol^{-1}, V_{m} is the gas mole volume, and Q is the total quantity of electric charge.

The liquid products were determined by H NMR (JEOL JNM ECZ600R 600 MHz), in which 300 μL electrolyte was mixed with 300 μL D_2O and 10 μL diluent dimethyl sulfoxide (DMSO), wherein DMSO served as an internal standard. The concentration of liquid products was calculated based on the following:

1220 | *J. Mater. Chem. A*, 2024, **12**, 1218–1232

This journal is © The Royal Society of Chemistry 2024

$$\frac{\frac{V_{DMSO} \times \rho_{DMSO} \times 10^{-3}}{M_{DMSO}} \times 6_{DMSO(H)}}{c_X \times 300 \times 10^{-6} \times n_{X(H)}} = \frac{1}{N}$$

where V is the volume of DMSO; ρ_{DMSO} is the density of DMSO (1.1 g cm^{-3} at 20 °C); M is the molar mass; c_X is the concentration of X product; $n_{X(H)}$ is the number of hydrogen atoms in the product X in the nuclear magnetic spectrum used to calculate the concentration of X; $\frac{1}{N}$ is the ratio of the product peak area to DMSO area in the nuclear magnetic spectrum.

The FE of liquid products was computed from:

$$FE = e \times F \times n/Q$$

where n is the total product (in moles).

Potentials were referenced to the RHE based on the following:

$$E_{RHE} = E \ (vs. \ Ag/AgCl) + 0.197 \ V + 0.059 \times pH$$

2.6 *In situ* Raman test

In situ Raman experiments were conducted by Confocal Raman Microscopy (Horiba) with a 785 nm near-infrared laser in a homemade electrolyzer cell. A platinum electrode and Ag/AgCl electrode were used as the counter and reference electrodes, respectively. The catalyst for the cathode was sprayed on carbon paper (0.5 × 1 cm^2) using ionomer solution as a binder. The electrolyte (1 M KCl) was saturated with CO$_2$ solution and CO$_2$ was continued to inject at a flow rate of 5 mL min^{-1}. A long focal length lens (Leica, 50×) was used for focusing and collecting the incident and scattered laser light. Electrolysis at different cathodic potentials was performed for 10 min before signal collection.

2.7 *In situ* ATR-IRAS measurement

In situ ATR-IRAS experiments were performed on a Nicolet iS20 spectrometer equipped with a HgCdTe (MCT/A) detector and a VeeMax III (PIKE Technologies) accessory in a homemade single-cell electrolyzer. A platinum electrode and Ag/AgCl electrode were used as the counter and reference electrodes. A fixed-angle Si prism (60°) coated with a catalyst embedded into the bottom of the cell served as the working electrode. Before testing, the detector was cooled with liquid nitrogen for at least 30 min to maintain a stable signal. Electrolysis at different cathodic potentials was carried out for 3 min with chronoamperometry by spectrum collection (32 scans, 4 cm^{-1} resolution). All spectra were subtracted from the background.

3. Results and discussion

3.1 Synthesis of catalysts and characterization analysis

As shown in Fig. 1, the synthesis of Cu$_2$O@SiO$_2$–NH$_2$ can be divided into three steps. Firstly, Cu$_2$O dodecahedron nanoparticles were synthesized by a precipitation method. Second, the Cu$_2$O NPs were mixed with TEOS uniformly, and the SiO$_2$

formed during the hydrolysis of TEOS is uniformly covered on the surface of Cu$_2$O NPs to form Cu$_2$O@SiO$_2$ samples. Finally, the Cu$_2$O@SiO$_2$ nanoparticles and ATPES were evenly dispersed with anhydrous ethanol to obtain Cu$_2$O@SiO$_2$–NH$_2$.[24] The detailed procedure is discussed in the Experimental section.

The morphology of the catalyst was characterized by SEM. As shown in Fig. 2a–c and S1,† the Cu$_2$O nanoparticles exhibit a regular dodecahedral shape. After SiO$_2$ coating, the surface of the nanoparticles becomes rough, indicating the successful coating of SiO$_2$, and there may be a porous structure (Fig. 2b and S1b†). In the subsequent modification process of –NH$_2$, the whole particle still maintained a complete dodecahedral structure. The results show that the SiO$_2$ coating and –NH$_2$ modification have no significant effect on the overall structure of Cu$_2$O nanoparticles (Fig. 2a–c and S1†). The structure of Cu$_2$O@SiO$_2$–NH$_2$ and control samples were characterized by TEM. As shown in Fig. S2,† the Cu$_2$O nanoparticle exhibits a smooth surface in the TEM image, and the high-resolution TEM (HR-TEM) image shows that there is a lattice fringe $d = 0.213$ nm on the catalyst surface, which is assigned to the Cu$_2$O (200) surface (Fig. S2b†). The Cu and O elements overlap with the STEM image in EDX element mapping (Fig. S2c†). In the TEM images of the Cu$_2$O@SiO$_2$ sample (Fig. S3a–c†), a lattice fringe of $d = 0.246$ nm can be seen in the inner layer, which belongs to the Cu$_2$O (111) crystal plane, and an amorphous SiO$_2$ coating with a thickness of about 10 nm located at the outer layer can be seen, which construct the obvious Cu$_2$O–SiO$_2$ interface. At the same time, the STEM and EDX element distribution maps further confirm the formation of the coating structure (Fig. S3d and e†). For the Cu$_2$O@SiO$_2$–NH$_2$ sample, a uniform coating layer with a thickness of about 13 nm can be seen on the surface of Cu$_2$O nanoparticles (Fig. 2a–f). By comparison with Cu$_2$O@SiO$_2$, it can be preliminarily confirmed that the Cu$_2$O@SiO$_2$ sample surface has been successfully modified with –NH$_2$. The lattice fringe of $d = 0.302$ nm of the Cu$_2$O (110) facet in close contact with the SiO$_2$–NH$_2$ coating layer in HR-TEM images (Fig. 2g) can confirm the formation of a Cu$_2$O–SiO$_2$–NH$_2$ interface. Furthermore, the EDX elemental maps show that the Si and N elements are mainly distributed on the surface of Cu$_2$O nanoparticles, and the overlay image of element distribution further proves the formation of Cu$_2$O@SiO$_2$–NH$_2$. The surface pore distribution on the surface of Cu$_2$O and Cu$_2$O@SiO$_2$–NH$_2$ catalysts was characterized by using N$_2$ isothermal adsorption–desorption curves. As illustrated in Fig. S4a,† the surface of Cu$_2$O exhibits almost no pore structure. In contrast, the N$_2$ isothermal adsorption–desorption curve of the Cu$_2$O@SiO$_2$–NH$_2$ catalyst reveals a gradual uptake of nitrogen gas with a hysteresis loop, indicating the presence of irregular pores on its surface. At the same time, combined with the pore size distribution diagram in Fig. S4b,† it shows that there are mesoporous pores with an average pore size of 3.32 nm distributed on the Cu$_2$O@SiO$_2$–NH$_2$ catalyst surface. And its specific surface area increases from 6 m^2 g^{-1} of Cu$_2$O to 40 m^2 g^{-1} of Cu$_2$O@SiO$_2$–NH$_2$.

X-ray diffraction (XRD) was conducted to analyze the chemical compositions of Cu$_2$O@SiO$_2$–NH$_2$ and the control samples. As shown in Fig. 3a and S5,† five obvious diffraction peaks in the XRD pattern of Cu$_2$O are located at $2\theta = 29°$, 36°, 42.5°, 62°

This journal is © The Royal Society of Chemistry 2024

J. Mater. Chem. A, 2024, **12**, 1218–1232 | **1221**

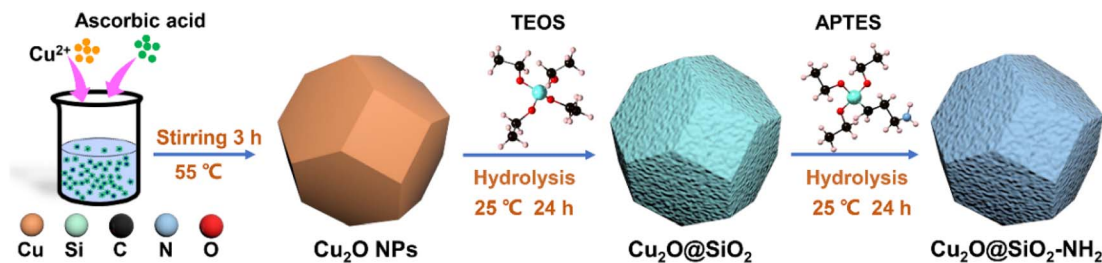**Fig. 1** The schematic illustration of the $Cu_2O@SiO_2-NH_2$ synthesis process.

and 74°, which belong to the (110), (111), (200), (220) and (311) crystal planes of Cu_2O, respectively. However, the position of the diffraction peaks of Cu_2O dodecahedron nanoparticles have no obvious change after SiO_2 coating and $-NH_2$ modification, indicating that the process of SiO_2 coating and $-NH_2$ modification have no significant effect on the crystal phase structure of Cu_2O nanoparticles. The surface chemical state of the samples was characterized by X-ray photoelectron spectroscopy (XPS). As shown in Fig. 3b, for the Cu 2p XPS spectrum, there are only two

peaks at the binding energies of 932.3 and 952.0 eV for the Cu_2O catalyst, which are ascribed to Cu^+ $2p_{3/2}$ and $2p_{1/2}$, respectively.[27] Meanwhile for $Cu_2O@SiO_2$ and $Cu_2O-SiO_2-NH_2$ catalysts, a satellite peak at 943 eV appears in the Cu 2p XPS spectra, indicating the presence of Cu^{2+} species.[28] Meanwhile, the asymmetric peaks of Cu 2p can be deconvoluted into two sets of peaks. The first group of peaks with binding energies of 932.3 and 952.0 eV are attributed to $2p_{3/2}$ and $2p_{1/2}$ of Cu^+ species. The second set of peaks at 934.6 and 954.3 eV belong to $2p_{3/2}$ and
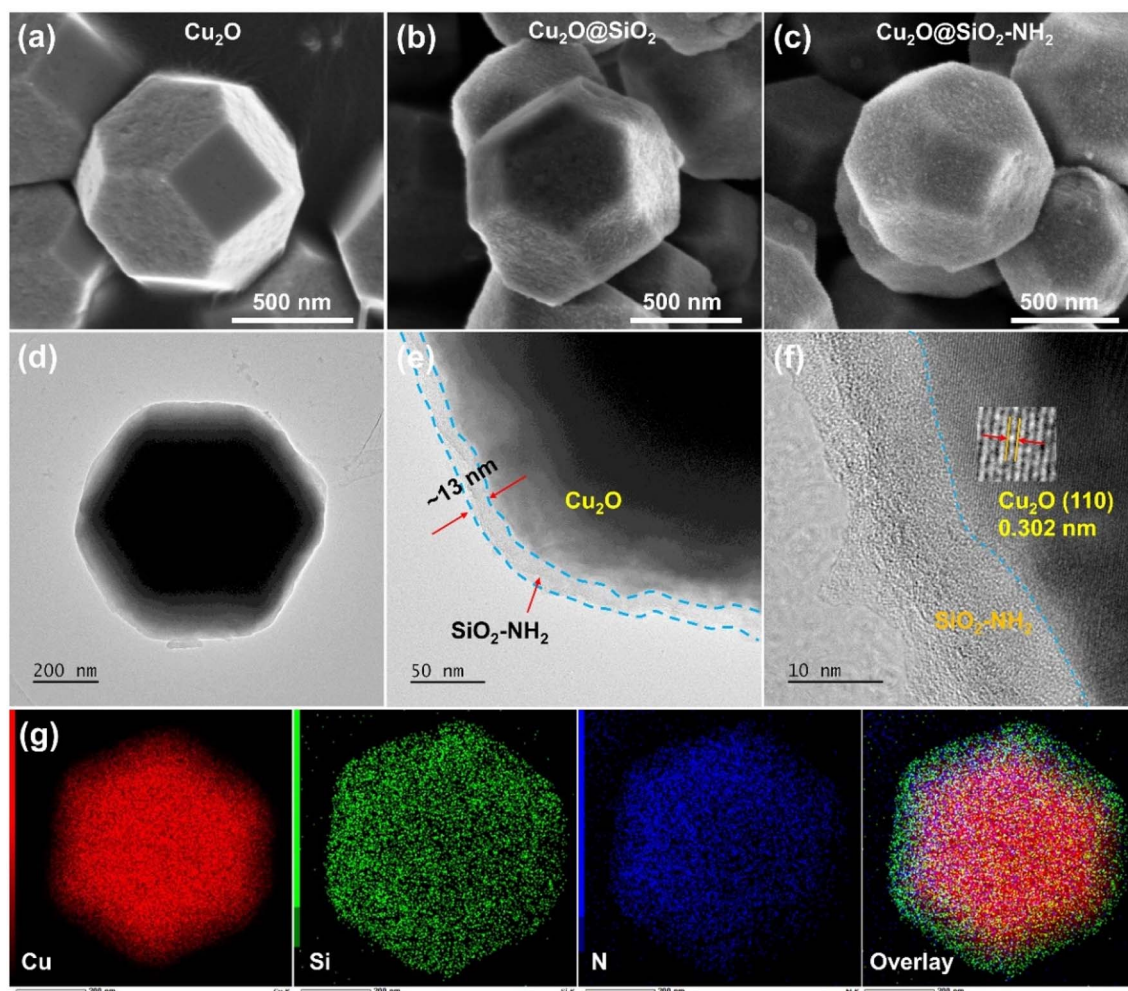

Fig. 2 The SEM images of (a) Cu_2O, (b) $Cu_2O@SiO_2$, and (c) $Cu_2O@SiO_2-NH_2$; and the structural characterization of $Cu_2O@SiO_2-NH_2$ (d and e) TEM images, (f) HR-TEM image and (g) EDX mapping.

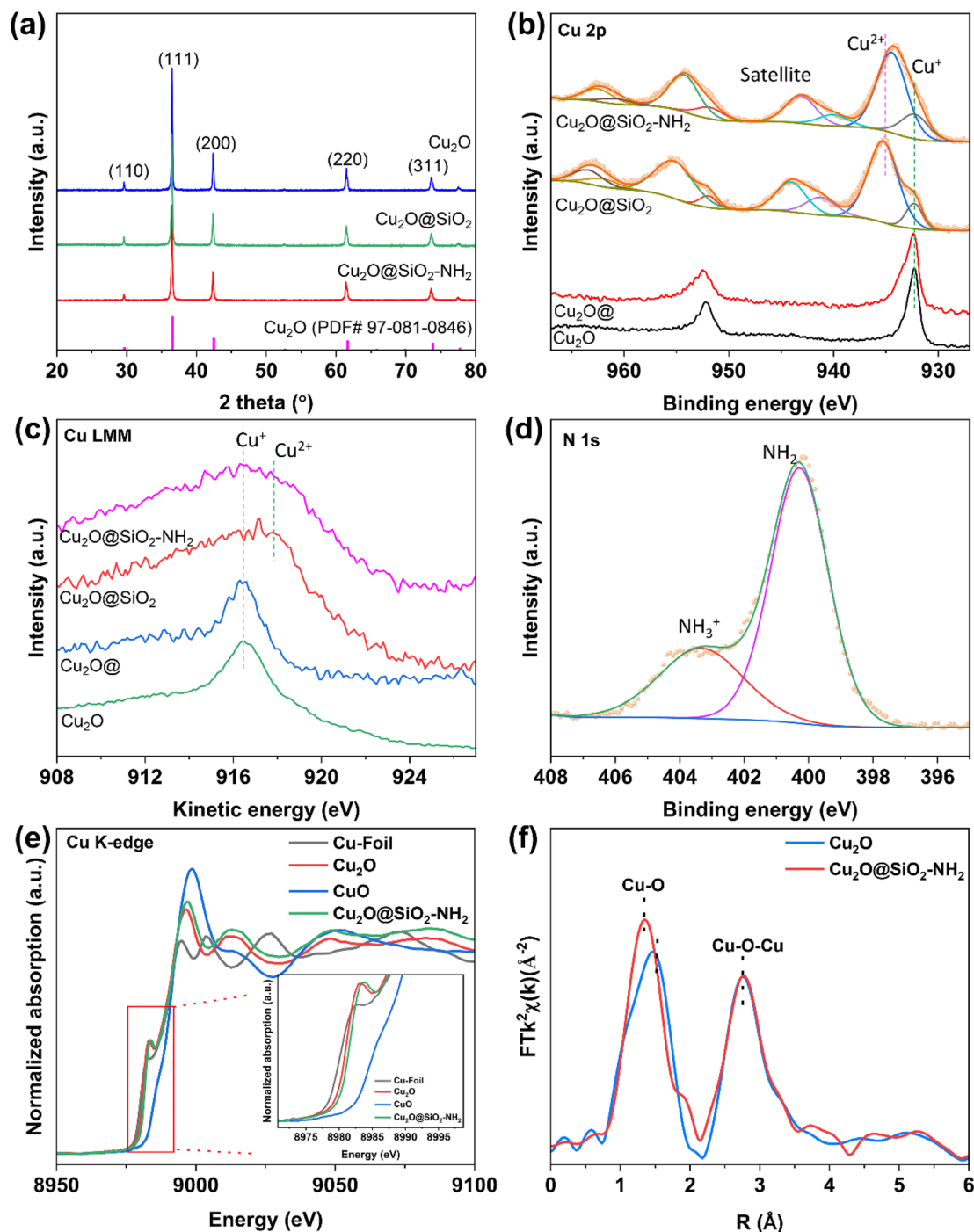**1222** | *J. Mater. Chem. A*, 2024, **12**, 1218–1232

This journal is © The Royal Society of Chemistry 2024

Fig. 3 Chemical composition characterization of Cu_2O, $Cu_2O@SiO_2$ and $Cu_2O@SiO_2–NH_2$. (a) XRD patterns, (b) Cu 2p XPS spectra, (c) Cu LMM XAES spectra, (d) N 1s XPS spectrum, (e) XANES spectra and (f) Fourier transformed EXAFS spectra of the Cu K-edge.

$2p_{1/2}$ of Cu^{2+} species.[29] Compared with Cu_2O, both Cu^{2+} and Cu^+ species exist on the surface of $Cu_2O@SiO_2$ and $Cu_2O@SiO_2–NH_2$, indicating strong interaction between SiO_2 and Cu species. This result is further confirmed by the Cu LMM X-ray induced Auger transition spectra (XAES) (Fig. 3c), where the Cu LMM XAES of Cu_2O sample shows a symmetrical peak at 916.8 eV, which belongs to Cu^+ species, while the Cu LMM XAES of $Cu_2O@SiO_2$ and $Cu_2O@SiO_2–NH_2$ show an asymmetric peak

with a wider full width at half maximum (FWHM), indicating the coexistence of Cu^+ and Cu^{2+} species at 916.8 and 917.9 eV.[30] As is well known, XRD is the analysis of the entire bulk phase, while XPS is surface analysis. No CuO phase is observed in the XRD pattern (Fig. 3a), indicating a low content of Cu^{2+}. XPS spectra (Fig. 3b) show a clear Cu^{2+} peak, indicating that Cu^{2+} is mainly present on the surface, while for $Cu_2O@SiO_2–NH_2$ and $Cu_2O@SiO_2$ catalysts, it is at the interface between Cu_2O and

SiO_2. The production of Cu^{2+} indicates that the strong interaction between SiO_2 and Cu_2O at the interface induces the oxidation effect of low valent Cu, which will affect the reduction of Cu_2O in the CO_2RR.[31] Moreover, XPS analysis was also performed on the $Cu_2O@$ sample that was treated under the same conditions without TEOS and APTES, and there is no significant difference in Cu 2p XPS between the $Cu_2O@$ and Cu_2O samples, which indicates that the treatment process did not oxidize Cu^+ to Cu^{2+}. Therefore, it can be confirmed that the strong interaction between SiO_2 and Cu species at the $Cu_2O–SiO_2$ interface promotes the formation of Cu^{2+} species. In addition, the chemical state of the $–NH_2$ group on the surface was characterized by N 1s XPS. As shown in Fig. 3d, the spectrum of N 1s XPS can be divided into two peaks located at the binding energies of 400 and 403.2 eV, respectively. According to a previous report, N 1s XPS at low binding energy belongs to the $–NH_2$ group, while the peak at high binding energy belongs to $–NH_3^+$.[32] This means that part of the $–NH_2$ group on $Cu_2O@SiO_2–NH_2$ has been protonated, which may increase the local pH on the catalyst surface.[22]

To explore more detailed structural information, the samples are further investigated by X-ray absorption fine structure spectroscopy (XAFS). Fig. 3e shows the X-ray absorption near-edge structure (XANES) spectra of Cu. In the Cu K-edge spectra, the pre-edge peak at 8987 eV is attributed to the dipole-forbidden 1s to 3d electron transition, which represents the fingerprint of Cu^{2+}. Moreover, the absorption edge of the curve located between those for Cu_2O and CuO shows the averaged valence state of Cu species in $Cu_2O@SiO_2–NH_2$ between +1 and +2, which is consistent with XPS data. Moreover, the extended X-ray absorption fine structure (EXAFS) spectra of the Cu K-edge show that compared to pure Cu_2O, the $Cu_2O@SiO_2–NH_2$ catalyst exhibits a shorter Cu–O bond length in the first shell, indicating that SiO_2 enhances the bonding between Cu^{2+}/Cu^+ and O (Fig. 3f). To demonstrate the interaction between $–NH_2$ groups and CO_2, the CO_2 adsorption capacity of the catalyst was tested. As shown in Fig. S6,† compared to $Cu_2O@SiO_2$, $Cu_2O@SiO_2–NH_2$ exhibits stronger CO_2 adsorption, indicating that the modification of $–NH_2$ significantly enhances the CO_2 adsorption capacity, which will play an important role in promoting the activity of the CO_2RR.

3.2 Electrochemical CO_2 reduction performance

The catalytic performance of $Cu_2O@SiO_2–NH_2$ for the CO_2RR was evaluated in a flow-cell with 1 M KCl cathode electrolyte (Fig. S7†). The gas and liquid phase products were detected by online gas chromatography (GC) and ^1H nuclear magnetic resonance (^1H NMR), respectively, (Fig. S8 and S9†). Fig. 4a shows the linear sweep voltammetry (LSV) curves of $Cu_2O@SiO_2–NH_2$ and the control samples. The cathode current density increases sharply after CO_2 gas is introduced, corresponding to the catalytic CO_2RR. When CO_2 is replaced by N_2, the cathodic current of $Cu_2O@SiO_2–NH_2$ decreases significantly, which indirectly indicates the low HER activity of $Cu_2O@SiO_2–NH_2$. Under a N_2 atmosphere, the HER current density of the $Cu_2O@SiO_2–NH_2$ catalyst is relatively low compared to

Cu_2O. Another possible reason is that the modification of SiO_2 and $–NH_2$ groups hinders the diffusion of H_2O molecules to the catalyst surface, while the CO_2 atmosphere eliminates this obstacle and accelerates the adsorption and diffusion of H_2O and CO_2. The current density of the CO_2RR on $Cu_2O@SiO_2–NH_2$ is significantly higher than that on Cu_2O and $Cu_2O@SiO_2$, suggesting that $Cu_2O@SiO_2–NH_2$ has a strong CO_2RR activity. Due to the exposure of the Cu_2O catalyst to the electrolyte solution, its HER current density under the N_2 atmosphere is slightly higher than that of $Cu_2O@SiO_2$ and $Cu_2O@SiO_2–NH_2$, indicating that the HER is more likely to occur in the Cu_2O catalyst.

The product distribution of the CO_2RR over $Cu_2O@SiO_2–NH_2$ and the control samples in the cathode potential range of $−1.1$ to $−1.9$ V as shown in Fig. 4b–d. The total FE of C_{2+} products exhibits a volcanic trend relative to the cathodic potential change over $Cu_2O@SiO_2–NH_2$ (Fig. 4b), and the total current density increases from 80 to 375 mA cm^{-2} (Fig. S10†). Under a current density of 292 mA cm^{-2} at $−1.7$ V, the FE of C_{2+} products reaches the highest value of 81.2% (including C_2H_4: 40.2%, C_2H_5OH: 29%, CH_3COOH: 9%, and C_3H_7OH: 3%), which has a higher activity than most reported catalysts (Table S1†). The FE of H_2 and C_1 is only 12% and 6%, respectively. In comparison, the FE of C_{2+} is 68.3% (C_2H_4: 35%, C_2H_5OH: 24.3%, CH_3COOH: 6.5%, and C_3H_7OH: 2.5%) over $Cu_2O@SiO_2$ at $−1.7$ V (Fig. 4c). Meanwhile for Cu_2O dodecahedron nanoparticles, the C_{2+} FE of Cu_2O is only 61.7% (C_2H_4: 31%, C_2H_5OH: 21%, CH_3COOH: 7%, and C_3H_7OH: 2.7%) at the optimum potential of $−1.6$ V (Fig. 4d). As a result, the ratio of C_{2+}/C_1 increases significantly from 4 in Cu_2O to 13.5 in $Cu_2O@SiO_2–NH_2$ (Fig. S11a†). In addition, the partial current densities of C_{2+} products of different samples increase from 147 mA cm^{-2} of Cu_2O to 168 mA cm^{-2} of $Cu_2O@SiO_2$ during the CO_2RR process, and then it further increases to 237 mA cm^{-2} over $Cu_2O@SiO_2–NH_2$ (Fig. 4e and S11b–d†). These results indicate that the $Cu_2O@SiO_2–NH_2$ catalyst has a high selectivity of C_{2+} products in the process of the CO_2RR.

By comparison, it can be found that when Cu_2O nanoparticles are coated with SiO_2, the HER is inhibited and the selectivity of C_{2+} products increases in the full cathodic potential range. This indicates that the SiO_2 coating layer helps to promote the C–C coupling process. According to the Cu 2p XPS results, the Cu species on the surface will maintain a high valence state after coating with SiO_2, thus improving the adsorption strength of *CO on Cu species and increasing the surface coverage of *CO,[33] followed by enhanced C–C coupling. After modifying the surface of the $Cu_2O@SiO_2$ sample with the $–NH_2$ group, the CO selectivity increases at low cathodic potential, indicating that the CO_2RR process is accelerated. According to previous reports, the interaction between nucleophilic N in $–NH_2$ and electrophilic C in CO_2 molecules can enrich CO_2, thus increasing the local CO_2 concentration on the catalyst surface,[22,34,35] and increasing the conversion rate of CO_2 to CO. Therefore, the reaction environment with a high local concentration of *CO can be provided at higher cathodic potential. Meanwhile, according to the N 1s XPS results (Fig. 3d), part of the $–NH_2$ group on the catalyst surface interacts with H_2O to
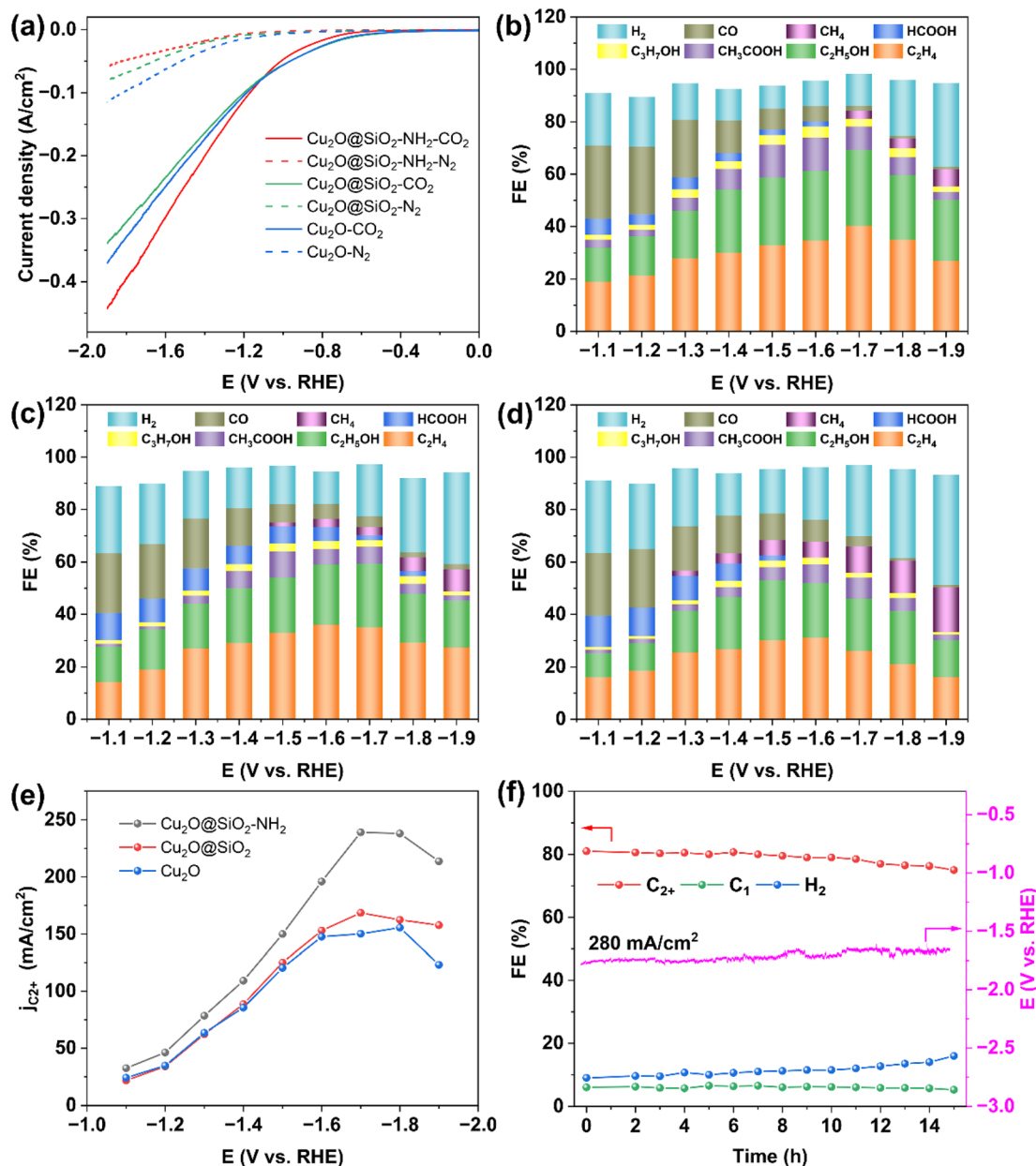
1224 | J. Mater. Chem. A, 2024, 12, 1218–1232

This journal is © The Royal Society of Chemistry 2024

Fig. 4 CO_2RR performance on $Cu_2O@SiO_2-NH_2$, $Cu_2O@SiO_2$ and Cu_2O catalysts. (a) LSV curves toward the CO_2RR; product distributions and corresponding faradaic efficiencies produced by $Cu_2O@SiO_2-NH_2$ (b), $Cu_2O@SiO_2$ (c), and Cu_2O (d), (e) the partial current density of C_{2+} products, and (f) stability test of $Cu_2O@SiO_2-NH_2$ at 280 mA cm^{-2} in 1 M KCl electrolyte.

form protonated $-NH_3^+$ and release OH^- at the same time, leading to a higher local pH value of the reaction micro-environment,[22] which is beneficial to promote the dimerization process of the C_1 intermediate.[36] Therefore, the positively charged Cu species coupled with the reaction microenvironment with sufficient CO supply and a high local pH value created by the surface $-NH_2$ group significantly enhance the formation of C_{2+} products from the CO_2RR and increase the FE of C_{2+} to 81.2% (Fig. 4b). However, in the Cu_2O catalyst without SiO_2 coating, the FE of CH_4 increases at high potential (Fig. 4d). According to a previous report, the CO_2RR is conducive to the formation of the C_1 product over the bulk Cu catalyst in neutral

electrolyte.[37,38] Therefore, it can be inferred that Cu_2O is rapidly reduced to form Cu in the reaction process, which leads to the formation of CH_4 and promotes the HER process at the same time, while the SiO_2 coating promotes the formation of C_{2+} by stabilizing the positively charged Cu species in the catalyst.[31] To eliminate the influence of the Cu/PTFE substrate on the analysis results, the CO_2RR performance of the Cu/PTFE substrate was tested under the same conditions. It is found that the CO_2RR to C_{2+} product conversion over Cu/PTFE shows a maximum FE of 26.2% at −1.5 V, and the FE of H_2 reaches 58% with a total current density of only 67 mA cm^{-2} (Fig. S12†). The partial current density of C_{2+} products over Cu/PTFE is only 17 mA

cm^{-2}, compared to 237 mA cm^{-2} over Cu$_2$O@SiO$_2$–NH$_2$, which shows that the main activity source of the CO$_2$RR to C$_{2+}$ products is originated from the target catalyst, and the Cu/PTFE substrate has little effect on the activity of the catalysts. The pH value of the electrolyte was also tested during the CO$_2$RR. Due to the generation of OH$^-$ at the cathode and the reaction of some OH$^-$ with CO$_2$ to generate CO$_3{}^{2-}$, the pH increased from 6.82 at 0 V to 10.11 at −1.9 V (Fig. S13†), and the local alkaline environment may facilitate C–C coupling.[2] In addition to the excellent FE of C$_{2+}$, Cu$_2$O@SiO$_2$–NH$_2$ also exhibits high stability at high current densities. The FE of C$_{2+}$ from the CO$_2$RR over Cu$_2$O@SiO$_2$–NH$_2$ does not decrease significantly for 15 h with 280 mA cm^{-2} current density in 1 M KCl electrolyte and remains above 75% (Fig. 4f).

3.3 Characterization of the samples after the activity test

Considering the reconstruction phenomenon of the oxidation state Cu-based catalyst during the CO$_2$RR, it is necessary to further explore the activity source of Cu$_2$O@SiO$_2$–NH$_2$ and the control samples, so the structure and composition of the samples after the activity test were characterized (the samples after the test were stored in a vacuum). As shown in TEM images of Fig. S14–S16,† the morphologies of Cu$_2$O@SiO$_2$–NH$_2$ and Cu$_2$O@SiO$_2$ catalysts have no obvious change after the CO$_2$RR, except that the thickness of the SiO$_2$–NH$_2$ layer slightly decreases, indicating that the coating layer is partially dissolved during the reaction. It can be explained by the fact that the formation of OH$^-$ during the CO$_2$RR increases the pH of the solution, and SiO$_2$ reacts with OH$^-$ leading to a decrease in the coating layer thickness. Meanwhile, the HR-TEM images of Cu$_2$O@SiO$_2$–NH$_2$ and Cu$_2$O@SiO$_2$ samples (Fig. S14c, d and S15c, d†) show lattice fringes of d = 0.302, 0.213 and 0.209 nm, which belong to the (110) and (200) of Cu$_2$O and Cu (111) crystal facets, respectively. This indicates that the oxidation state Cu on the catalyst surface is partially reduced, forming the Cu–Cu$_2$O interface; therefore, the metal-oxide interface effect can effectively improve the formation rate of C$_{2+}$ from the CO$_2$RR.[20] At the same time, the elements overlap each other in the EDX mapping of Cu$_2$O@SiO$_2$–NH$_2$ and Cu$_2$O@SiO$_2$ samples, which proves that the Cu$_2$O@SiO$_2$–NH$_2$ catalyst still maintains a complete coating structure after the CO$_2$RR (Fig. S14e, f and S15e†). In contrast, the morphology of the Cu$_2$O catalyst after the CO$_2$RR is significantly changed (Fig. S16a and b†), and only the lattice fringe of the Cu (111) facet (d = 0.2086 nm) can be observed in the HR-TEM image (Fig. S16c†). This indicates that Cu$_2$O nanoparticles are completely reduced to Cu during the CO$_2$RR. Notably, irregular holes can be observed on the surface of Cu$_2$O nanoparticles (Fig. S16d†), which further indicates that Cu$_2$O nanoparticles are reduced, leading to a change in the morphology of nanoparticles. The EDX mapping also confirmed the morphology change (Fig. S16e†), where the Cu element is not evenly distributed. By comparing the TEM images of Cu$_2$O@SiO$_2$–NH$_2$, Cu$_2$O@SiO$_2$ and Cu$_2$O catalysts, the results indicate that SiO$_2$ coating can stabilize the morphology of Cu$_2$O nanoparticles, inhibit the reduction of oxidized Cu in the catalyst, and form a stable metal-oxide interface in the

reduction process, which accelerates the C–C coupling step during the CO$_2$RR.

XRD characterization was carried out to analyze the chemical composition of the catalyst after the CO$_2$RR. As shown in Fig. 5a, there is only one diffraction peak at $2\theta = 43.2°$ in the XRD pattern of the Cu$_2$O catalyst, which is attributed to metal Cu (PDF# 97-004-3493), indicating that Cu$_2$O is completely reduced during the CO$_2$RR. There are two sets of diffraction peaks in the XRD patterns of Cu$_2$O@SiO$_2$–NH$_2$ and Cu$_2$O–SiO$_2$ catalysts, which are located at $2\theta = 36.4°$, $42.5°$ and $2\theta = 43.2°$. They belong to the Cu$_2$O (PDF# 97-018-0846) and Cu phases, respectively. The XRD results show that Cu$_2$O nanoparticles coated with SiO$_2$ inhibit the reduction of Cu$^+$ species and form a metal-oxide interface in the CO$_2$RR process. Combined with TEM characterization results, it is further demonstrated that SiO$_2$ coating is beneficial to stabilize the oxidized copper in Cu$_2$O nanoparticles during the CO$_2$RR, due to the strong interaction between SiO$_2$ and Cu$_2$O species. At the same time, the Cu 2p XPS spectrum of Cu$_2$O after the CO$_2$RR (Fig. 5b) shows only two peaks located at 932.0 and 951.8 eV, belonging to Cu^0 species.[39] Meanwhile for Cu 2p XPS of Cu$_2$O@SiO$_2$ and Cu$_2$O@SiO$_2$–NH$_2$, there is weak satellite peaks at 942–944 eV and acromial peaks at 934.7 eV, indicating the presence of a small amount of Cu^{2+} on the surface.[40] We further analyzed the Cu LMM XAES spectra of Cu$_2$O@SiO$_2$–NH$_2$ and control samples after the CO$_2$RR. As shown in Fig. 5c, there is only one peak located at 918.1 eV in the Cu LMM XAES of the Cu$_2$O catalyst, which belongs to Cu^0 species, suggesting that all Cu$^+$ species are reduced to Cu^0 species. In contrast, the Cu LMM XAES of Cu$_2$O@SiO$_2$ and Cu$_2$O@SiO$_2$–NH$_2$ catalysts can be fitted into two peaks at 916.2 and 918.1 eV, belonging to the Cu$^+$ and Cu^0 species, respectively.[19,41] Compared with the Cu 2p XPS before the CO$_2$RR (Fig. 3b), the surface of the Cu$_2$O@SiO$_2$–NH$_2$ catalyst is mainly Cu^{2+}, and after the CO$_2$RR, it is mainly mixed Cu$^+$ and Cu^0, indicating that SiO$_2$ can stabilize part of Cu$^+$ and form Cu$^+$–Cu^0 interfaces. The results are consistent with TEM and XRD images. Meanwhile, the Si 2p XPS also can be detected in Cu$_2$O@SiO$_2$–NH$_2$ and Cu$_2$O@SiO$_2$ catalysts, which confirms the presence of SiO$_2$ on the catalyst surface after the CO$_2$RR (Fig. S17†). Moreover, the N 1s XPS spectrum shows the retention of –NH$_2$ groups on the surface and the presence of groups in two states of –NH$_2$ and –NH$_3{}^+$, indicating that the surface –NH$_2$ continued to play a role in the enrichment of CO$_2$ during the reaction process and accelerated the conversion rate of CO$_2$ (Fig. 5d).

3.4 Reaction mechanism study

In situ Raman experiments were performed to study the valence changes of Cu species of Cu$_2$O@SiO$_2$–NH$_2$ and control samples, and to detect the key intermediates in the CO$_2$RR process. As shown in Fig. 6, under open-circuit potential conditions, the two Raman peaks at 145 and 213 cm^{-1} belong to the Cu$_2$O phase.[13] When the cathodic potential is applied, the peaks of the Cu$_2$O phase still exist in the Raman spectrum of Cu$_2$O@SiO$_2$–NH$_2$, indicating that the Cu$^{\delta+}$ species can be well preserved in the CO$_2$RR process. Similarly, this phenomenon

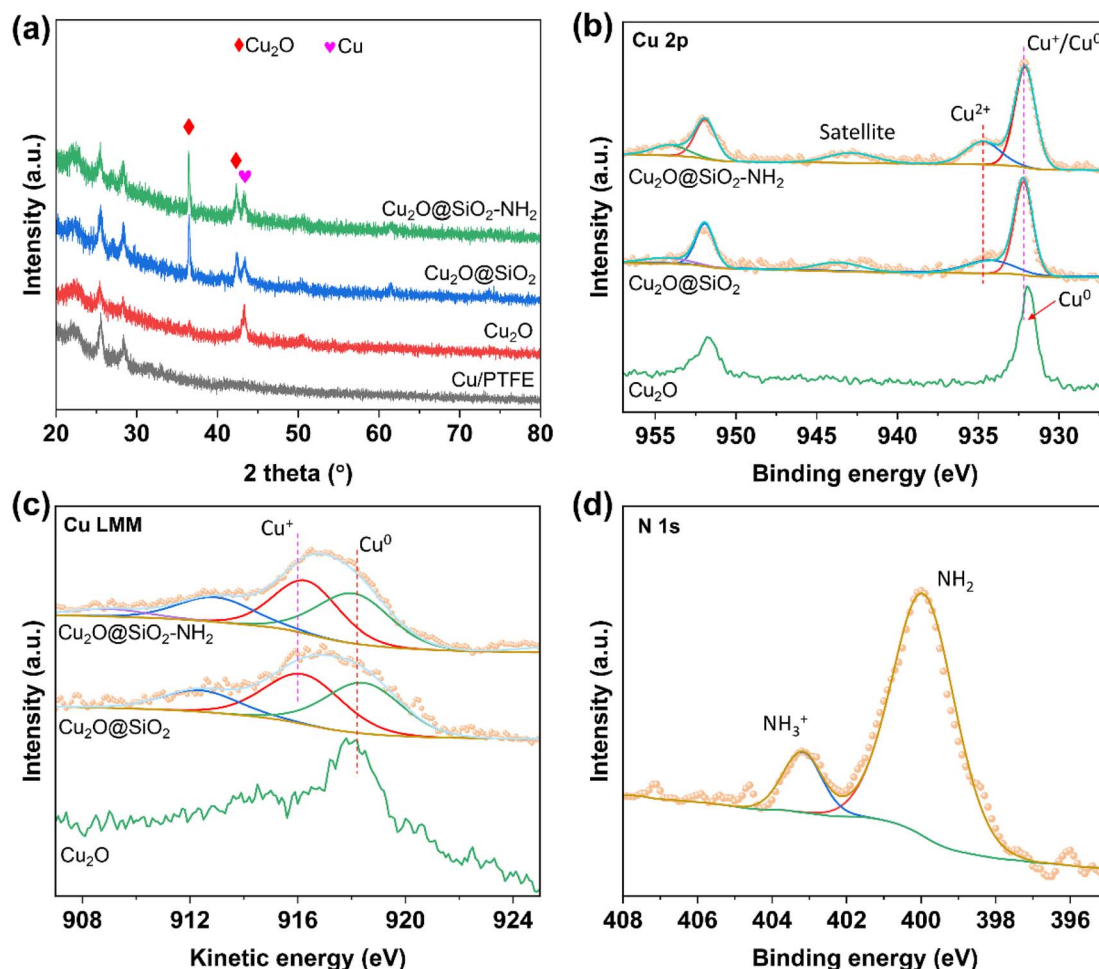**Fig. 5** Chemical composition characterizations of Cu_2O, $Cu_2O@SiO_2$ and $Cu_2O@SiO_2–NH_2$ after the CO_2RR. (a) XRD patterns, (b) Cu 2p XPS spectra, (c) Cu LMM XAES spectra and (d) N 1s XPS spectrum.

has also been observed on the $Cu_2O@SiO_2$ catalyst, where Cu_2O species can exist stably with the increase of cathodic potential. In contrast, for the Cu_2O catalyst, the two Raman peaks at 145 and 213 cm^{-1} only can be observed under the open-circuit potential conditions. However, when a cathodic potential of -1.1 V is applied, the two peaks disappear, suggesting that the Cu_2O on the catalyst surface is completely reduced to metal Cu. The above analysis results imply that the strong interaction between SiO_2 and Cu_2O can improve the stability of $Cu^{\delta+}$ species on the catalyst surface. This is consistent with the results of TEM and XRD of samples after the CO_2RR. More importantly, in the Raman spectrum of $Cu_2O@SiO_2–NH_2$, an obvious peak at 529 cm^{-1} is observed, which is related to the chemisorption of CO_2 on the copper surface ($*CO_{2ad}$),[42,43] and it further enhances with the increase of cathodic potential applied. This shows that the catalyst has strong CO_2 adsorption and activation ability (Fig. 6a). In contrast, the peak intensity of $*CO_{2ad}$ at 529 cm^{-1} on $Cu_2O@SiO_2$ and Cu_2O catalysts decreases sharply (Fig. 6b and c), indicating that $*CO_{2ad}$ is less adsorbed on the surface. Therefore, this result shows that $–NH_2$ enhances the ability of the catalyst to adsorb and activate CO_2. As mentioned above, the

$–NH_2$ group can enrich CO_2 molecules, thus improving the CO_2 coverage on the catalyst surface.[22]

Moreover, the peaks at 297 and 373 cm^{-1} are attributed to the rotation and stretching vibrations of $*CO$ on Cu (Cu–CO) in the Raman spectra,[12,44] which indicate the formation of CO and the adsorption of $*CO$ on the catalyst surface (Fig. 6a–c). At the same time, the most obvious peak at 2000–2080 cm^{-1} is associated with $*CO_a$ (Fig. 6d).[27] It is worth noting that the adsorption peak of $*CO$ first increases and then decreases with the increase of cathodic potential, indicating that the coverage of $*CO$ on the catalyst surface increases first with the cathodic potential, which promotes the C–C coupling step. However, after the C–C coupling reaction, the $*CO$ adsorbed on the surface will be consumed, thus weakening the adsorption peak of $*CO$.[44] In contrast, the Cu–CO Raman signal on $Cu_2O@SiO_2$ is weaker (Fig. 6b and e), indicating the low surface coverage of $*CO$. Moreover, the Cu–CO Raman signal is the weakest on the Cu_2O catalyst (Fig. 6c and f). The results of *in situ* Raman show that the interaction between $–NH_2$ and CO_2 creates a high local concentration of the CO_2 microenvironment at the Cu^0–Cu^+–NH_2 composite interfaces, which accelerates the activation of CO_2 and generation of CO, and enhances the adsorption of

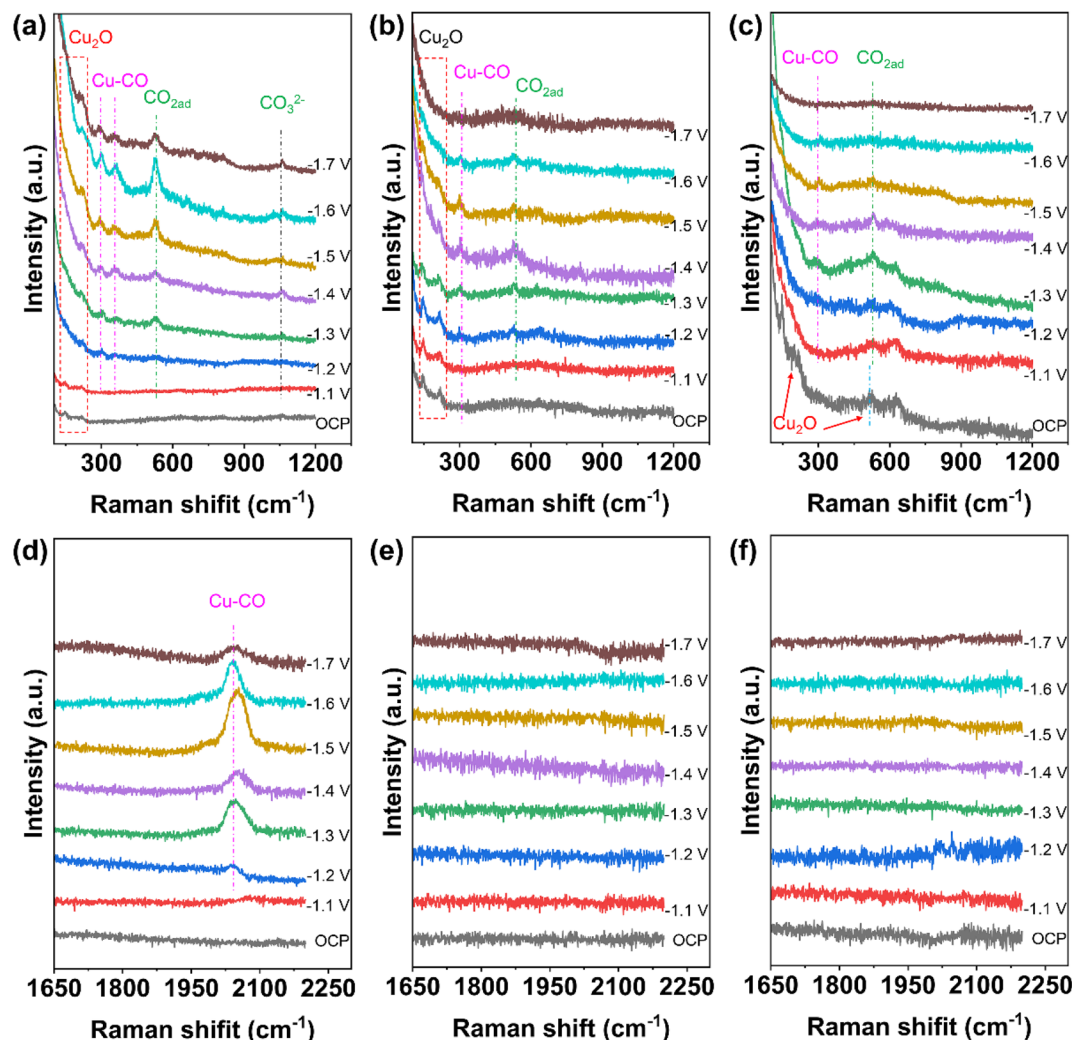**Fig. 6** *In situ* Raman spectra of the catalysts under CO$_2$RR conditions. (a and d) Cu$_2$O@SiO$_2$−NH$_2$, (b and e) Cu$_2$O@SiO$_2$, and (c and f) Cu$_2$O.

*CO.[45] At the same time, the Cu^0/Cu$^+$ synergistic effect at the interface may promote the C–C coupling step. However, the Cu^0–Cu$^+$ interface without –NH$_2$ on the Cu$_2$O@SiO$_2$ surface leads to a low local concentration of the CO$_2$ microenvironment, which suppresses the CO generation rate, followed by a slow C–C coupling step. The lack of a SiO$_2$ coating layer on the Cu$_2$O catalyst leads to the quick reduction of Cu$_2$O to metal Cu, thus reducing the adsorption strength of CO.

In situ attenuated total reflectance-infrared absorption spectroscopy (ATR-IRAS) was carried out under CO$_2$RR conditions to monitor the adsorption intermediates and get insight into the CO$_2$RR mechanism more precisely. As shown in Fig. 7, when the applied cathodic potential is higher than −1.1 V, new infrared (IR) absorption peaks begin to appear in the ATR-IRAS of all catalysts. The most obvious peak appears at 1650 cm^{-1} in the ATR-IRAS of Cu$_2$O@SiO$_2$−NH$_2$ and Cu$_2$O@SiO$_2$ (Fig. 7a, b), which is related to the IR absorption peak of H$_2$O.[46] The intensity of the IR absorption peak increases with the increase of cathodic potential, indicating that the process of H$_2$O adsorption and activation is accelerated at high cathodic

potential. In contrast, on the surface of the Cu$_2$O catalyst, the intensity of this absorption peak decreases sharply. This suggests that the surface of Cu$_2$O@SiO$_2$ can promote the adsorption and activation of H$_2$O. This can be explained by the fact that the metal-oxide interface (Cu^0–Cu$^+$) can regulate the dissociation process of H$_2$O, resulting in high coverage of *H species on the catalyst surface.[47,48] The presence of a metal-oxide interface is also confirmed by the XRD and TEM results. From the CO$_2$RR equations in Table S2,† it can be seen that the CO$_2$RR must involve the participation of active *H, such as the transfer of 12 protons and 12 electrons to generate ethylene and ethanol, where the protons obtain electrons and become active *H. Therefore, the peak intensity of the H$_2$O peak represents the ability to activate H$_2$O to produce active *H, which is partially involved in the CO$_2$RR and partially in the HER. For catalysts with high CO$_2$RR activity, most of the active *H is involved in the CO$_2$RR. In contrast, for catalysts with poor CO$_2$RR activity, most of the active *H is involved in the HER. From Table S2,† it can also be seen that the number of electrons transferred is directly proportional to the number of protons consumed,
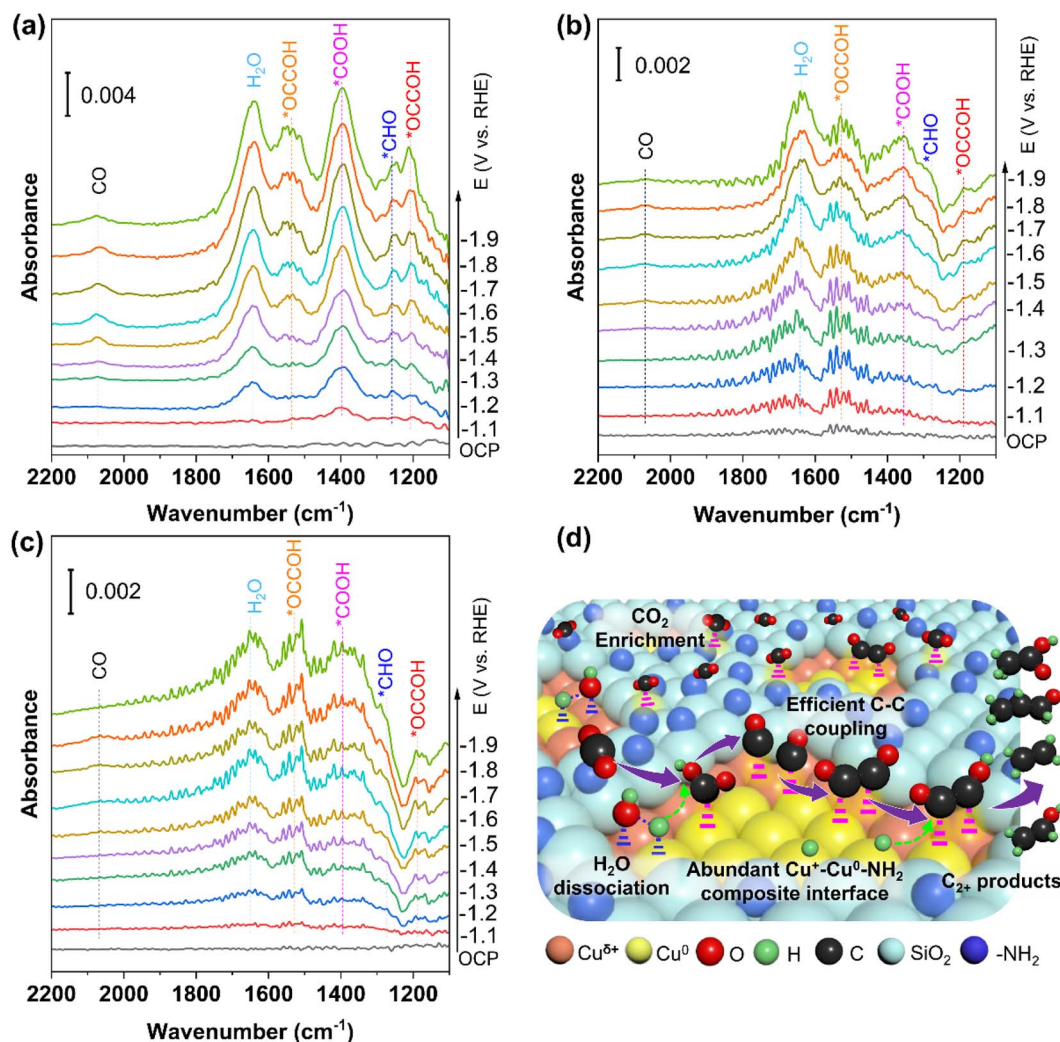
1228 | *J. Mater. Chem. A*, 2024, **12**, 1218–1232

This journal is © The Royal Society of Chemistry 2024

Fig. 7 *In situ* ATR-IRAS spectra of catalysts under CO_2RR conditions and the reaction mechanism. (a) $Cu_2O@SiO_2-NH_2$, (b) $Cu_2O@SiO_2$, and (c) Cu_2O and (d) reaction mechanism of the CO_2RR to C_{2+} product formation over the $Cu_2O@SiO_2-NH_2$ catalyst.

which means that the number of active *H is directly proportional to the current density. In Fig. S11,† the current density of C_{2+} in the CO_2RR process of the $Cu_2O@SiO_2-NH_2$ catalyst is 237 mA cm^{-2}, and the current density of H_2 is only 35.32 mA cm^{-2}, while for the Cu_2O catalyst, the current density of C_{2+} is only 147 mA cm^{-2}, but the current density of H_2 is 76.55 mA cm^{-2}. From this result, it can be seen that more active *H is generated in the $Cu_2O@SiO_2-NH_2$ catalyst, and most of it is involved in the CO_2RR, and the HER current density of Cu_2O is high, the total current density is low, resulting in less active *H, which is consistent with the H_2O peak intensity in the ATR-IRAS spectra.

In addition to the H_2O absorption peak, the other strong peak located at 1390 cm^{-1} belongs to the *COOH species,[49] implying that the $Cu_2O@SiO_2-NH_2$ catalyst has strong adsorption and activation ability for CO_2 molecules. The simultaneous adsorption and activation of H_2O and CO_2 molecules indicate a good coupling between H_2O dissociation and CO_2 reduction. The activated *CO_2 species and surface *H_{ad} species promote the formation of *CO species, which can be confirmed by the

*CO absorption peak appearing around 2070 cm^{-1} in the ATR-IRAS spectrum.[46] There is an obvious *CO IR absorption peak on the $Cu_2O@SiO_2-NH_2$ surface, indicating the high coverage of *CO on the $Cu_2O@SiO_2-NH_2$ surface, which promotes the formation of C_{2+} products (Fig. 7a). In contrast, the ATR-IRAS of $Cu_2O@SiO_2$ shows a weak *CO IR absorption peak, which corresponds to a low CO coverage (Fig. 7b). However, no obvious IR absorption peak of *CO was found on the surface of Cu_2O, indicating weak *CO adsorption capacity on the surface, because Cu_2O was reduced to Cu^0, followed by low *CO coverage (Fig. 7c). This finding proves that the presence of $-NH_2$ can improve the adsorption and activation of CO_2 on the catalyst surface, and the Cu^+ species can promote the adsorption of CO, thus improving the surface coverage of *CO.

In addition, the peaks of ATR-IRAS at 1260 cm^{-1}, 1205 cm^{-1}, and 1530 cm^{-1} are related to the intermediate species of *CHO and *OCCOH on the catalyst, respectively (Fig. 7).[49] The absorption peak intensity of *OCCOH increases with the cathodic potential, which is consistent with the enhancement

trend of the C_{2+} product formation rate with the change of the cathodic potential. Compared with $Cu_2O@SiO_2$ and Cu_2O catalysts, the IR absorption peak of the C_2 intermediate on $Cu_2O@SiO_2$–NH_2 is more intense, indicating that the C_2 intermediate has a stable adsorption structure on the catalyst surface, which is conducive to promoting C–C coupling, followed by higher C_{2+} product selectivity. Therefore, on the surface of $Cu_2O@SiO_2$–NH_2, the enhancement of the CO_2 adsorption activation process improves the surface coverage of *CO, thus accelerating the C–C coupling process. The high coverage of *H_{ad} species can enhance the protonation process of C_{2+} intermediates and desorption of products, thus promoting the efficient formation of C_{2+} products from the CO_2RR process.[50,51]

According to the above analysis results, the CO_2RR mechanism on the surface of $Cu_2O@SiO_2$–NH_2 can be reasonably proposed (Fig. 7d). Firstly, CO_2 reaches the three-phase reaction interface through the gas diffusion layer, and then is enriched by –NH_2 at the Cu^0–Cu^+–NH_2 composite interfaces, forming a local microenvironment with a high concentration of CO_2.[34] CO_2 molecules diffused through the porous SiO_2 coating layer to reach the Cu^0–Cu^+ interface, and adsorbed and activated at the active site to form *CO_{2ad}. At the same time, the H_2O molecules are activated by the Cu^0–Cu^+ interface to increase the concentration of *H, which couples with CO_2 activation to form *COOH, and promotes the formation of *CO. Then the Cu^+ enhances the adsorption of *CO, which facilitate the C–C coupling process at the $Cu^{\delta+}/Cu^0$ interface. The C_2 intermediate is protonated by *H on the catalyst surface, which promotes product desorption and thus accelerates the formation of C_{2+} products. This mechanism is consistent with the theoretical calculation results reported in the literature. For example, the electron density around the C atoms in *CO on the Cu_2O–Cu interface is higher than that on Cu_2O, which reduces the reaction energy barrier of C–C coupling to form *OCCO. Meanwhile, the energy barrier of H_2O dissociation on Cu, Cu_2O, and Cu_2O–Cu is 2.33, 2.15, and 1.64 eV, respectively; therefore, the faster H_2O dissociation and promoted C–C coupling contribute to accelerated C_{2+} product formation from the CO_2RR on the Cu_2O–Cu interface.[48]

4. Conclusion

In this work, dodecahedral $Cu_2O@SiO_2$–NH_2 nanoparticles have been synthesized by hydrolysis of TEOS and APTES on the surface of Cu_2O particles for the CO_2RR to C_{2+} products. A series of characterization results show electronic interaction between Cu_2O and SiO_2–NH_2, and the Cu^0–Cu^+–NH_2 composite interface is formed in the CO_2RR process. With the help of the interface effect, the FE of C_{2+} products reaches 81.3% with a current density of 290 mA cm^{-2}, and is stable for 15 h without significant degradation of activity. Combined with XPS and *in situ* Raman spectroscopy, the high activity and stability originate from the interaction between SiO_2 and Cu_2O, which stabilizes the positively charged Cu species and creates a stable Cu^0–Cu^+ interface under CO_2RR conditions. Meanwhile, the surface –NH_2 can enrich CO_2 and promote the adsorption and activation

of CO_2 on the catalyst surface, which accelerates the formation of *CO; the –NH_2 protonation process increases the local pH, which creates a reaction microenvironment that facilitates C–C coupling at the Cu^0–Cu^+–NH_2 composite interface, and improves the efficiency of the CO_2RR to C_{2+}. This research provides a new idea for the surface modification of Cu-based catalysts and the design of an efficient Cu^0–Cu^+–NH_2 composite interface.

Author contributions

Conceptualization: Z.-L. W.; methodology: Z.-Y. Z. and H. T.; software: H. T.; validation: Z.-Y. Z. and H. J.; formal analysis: X. W., L. B., and Y. L.; investigation: Y. L. and N. K.; resources: Z.-L. W.; data curation: all authors; writing – original draft: all authors; writing – review & editing: all authors; visualization: Z.-Y. Z. and Z.-L. W.; supervision: Y. Y. and Z.-L. W.; project administration: Y. Y. and Z.-L. W.; funding acquisition: N. K., Y. Y., and Z.-L. W.

Conflicts of interest

There are no conflicts to declare.

Acknowledgements

References

1 S. Nitopi, E. Bertheussen, S. B. Scott, X. Liu, A. K. Engstfeld, S. Horch, B. Seger, I. E. L. Stephens, K. Chan, C. Hahn, J. K. Nørskov, T. F. Jaramillo and I. Chorkendorff, *Chem. Rev.*, 2019, **119**, 7610–7672.

2 S. Garg, M. Li, A. Z. Weber, L. Ge, L. Li, V. Rudolph, G. Wanga and T. E. Rufford, *J. Mater. Chem. A*, 2020, **8**, 1511–1544.

3 Y. Lei, Z. Wang, A. Bao, X. Tang, X. Huang, H. Yi, S. Zhao, T. Sun, J. Wang and F. Gao, *Chem. Eng. J.*, 2023, **453**, 139663.

4 Y. Hori, A. Murata and R. Takahashi, *J. Chem. Soc., Faraday Trans. 1*, 1989, **85**, 2309–2326.

5 M. Fang, M. Wang, Z. Wang, Z. Zhang, H. Zhou, L. Dai, Y. Zhu and L. Jiang, *J. Am. Chem. Soc.*, 2023, **145**, 11323–11332.

6 Z.-Y. Zhang, H. Tian, L. Bian, S.-Z. Liu, Y. Liu and Z.-L. Wang, *J. Energy Chem.*, 2023, **83**, 90–97.

7 L. Fan, C. Xia, F. Yang, J. Wang, H. Wang and Y. Lu, *Sci. Adv.*, 2020, **6**, eaay3111.

8 A. Bagger, W. Ju, A. S. Varela, P. Strasser and J. Rossmeisl, *ChemPhysChem*, 2017, **18**, 3266–3273.

1230 | *J. Mater. Chem. A*, 2024, **12**, 1218–1232

This journal is © The Royal Society of Chemistry 2024

9 P.-P. Yang, X.-L. Zhang, P. Liu, D. J. Kelly, Z.-Z. Niu, Y. Kong, L. Shi, Y.-R. Zheng, M.-H. Fan, H.-J. Wang and M.-R. Gao, *J. Am. Chem. Soc.*, 2023, **145**, 8714–8725.

10 H. Li, Y. Jiang, X. Li, K. Davey, Y. Zheng, Y. Jiao and S.-Z. Qiao, *J. Am. Chem. Soc.*, 2023, **145**, 14335–14344.

11 D. Zhong, D. Cheng, Q. Fang, Y. Liu, J. Li and Q. Zhao, *Chem. Eng. J.*, 2023, **470**, 143907.

12 J. Zhang, Y. Wang, Z. Li, S. Xia, R. Cai, L. Ma, T. Zhang, J. Ackley, S. Yang, Y. Wu and J. Wu, *Adv. Sci.*, 2022, **9**, 2200454.

13 S. Mu, H. Lu, Q. Wu, L. Li, R. Zhao, C. Long and C. Cui, *Nat. Commun.*, 2022, **13**, 3694.

14 Y. Jiang, X. Wang, D. Duan, C. He, J. Ma, W. Zhang, H. Liu, R. Long, Z. Li, T. Kong, X. J. Loh, L. Song, E. Ye and Y. Xiong, *Adv. Sci.*, 2022, **9**, 2105292.

15 Y. Zhou, Y. Liang, J. Fu, K. Liu, Q. Chen, X. Wang, H. Li, L. Zhu, J. Hu, H. Pan, M. Miyauchi, L. Jiang, E. Cortes and M. Liu, *Nano Lett.*, 2022, **22**, 1963–1970.

16 Y. Zhou, F. Che, M. Liu, C. Zou, Z. Liang, P. De Luna, H. Yuan, J. Li, Z. Wang, H. Xie, H. Li, P. Chen, E. Bladt, R. Quintero-Bermudez, T.-K. Sham, S. Bals, J. Hofkens, D. Sinton, G. Chen and E. H. Sargent, *Nat. Chem.*, 2018, **10**, 974–980.

17 P. De Luna, R. Quintero-Bermudez, C.-T. Dinh, M. B. Ross, O. S. Bushuyev, P. Todorović, T. Regier, S. O. Kelley, P. Yang and E. H. Sargent, *Nat. Catal.*, 2018, **1**, 103–110.

18 K. Hadjiivanov and H. Knözinger, *Phys. Chem. Chem. Phys.*, 2001, **3**, 1132–1137.

19 Y. Zhou, Y. Yao, R. Zhao, X. Wang, Z. Fu, D. Wang, H. Wang, L. Zhao, W. Ni, Z. Yang and Y.-M. Yan, *Angew. Chem., Int. Ed.*, 2022, **61**, e202205832.

20 Y. Zang, T. Liu, P. Wei, H. Li, Q. Wang, G. Wang and X. Bao, *Angew. Chem., Int. Ed.*, 2022, **134**, e202209629.

21 F. Li, A. Thevenon, A. Rosas-Hernández, Z. Wang, Y. Li, C. M. Gabardo, A. Ozden, C. T. Dinh, J. Li, Y. Wang, J. P. Edwards, Y. Xu, C. McCallum, L. Tao, Z.-Q. Liang, M. Luo, X. Wang, H. Li, C. P. O'Brien, C.-S. Tan, D.-H. Nam, R. Quintero-Bermudez, T.-T. Zhuang, Y. C. Li, Z. Han, R. D. Britt, D. Sinton, T. Agapie, J. C. Peters and E. H. Sargent, *Nature*, 2020, **577**, 509–513.

22 X. Chen, J. Chen, N. M. Alghoraibi, D. A. Henckel, R. Zhang, U. O. Nwabara, K. E. Madsen, P. J. A. Kenis, S. C. Zimmerman and A. A. Gewirth, *Nat. Catal.*, 2021, **4**, 20–27.

23 Z.-Z. Wu, X.-L. Zhang, Z.-Z. Niu, F.-Y. Gao, P.-P. Yang, L.-P. Chi, L. Shi, W.-S. Wei, R. Liu, Z. Chen, S. Hu, X. Zheng and M.-R. Gao, *J. Am. Chem. Soc.*, 2022, **144**, 259–269.

24 L. Li, W. Gu, J. Liu, S. Yan and Z. P. Xu, *Nano Res.*, 2015, **8**, 682–694.

25 P.-P. Yang, X.-L. Zhang, P. Liu, D. J. Kelly, Z.-Z. Niu, Y. Kong, L. Shi, Y.-R. Zheng, M.-H. Fan, H.-J. Wang and M.-R. Gao, *J. Am. Chem. Soc.*, 2023, **145**, 8714–8725.

26 W. Liu, P. Zhai, A. Li, B. Wei, K. Si, Y. Wei, X. Wang, G. Zhu, Q. Chen, X. Gu, R. Zhang, W. Zhou and Y. Gong, *Nat. Commun.*, 2022, **13**, 1877.

27 G.-Y. Duan, X.-Q. Li, G.-R. Ding, L.-J. Han, B.-H. Xu and S.-J. Zhang, *Angew. Chem., Int. Ed.*, 2022, **61**, e202110657.

28 X. Zhou, J. Shan, L. Chen, B. Y. Xia, T. Ling, J. Duan, Y. Jiao, Y. Zheng and S.-Z. Qiao, *J. Am. Chem. Soc.*, 2022, **144**, 2079–2084.

29 C. Azenha, C. Mateos-Pedrero, M. Alvarez-Guerra, A. Irabien and A. Mendes, *Chem. Eng. J.*, 2022, **445**, 136575.

30 H.-Q. Liang, S. Zhao, X.-M. Hu, M. Ceccato, T. Skrydstrup and K. Daasbjerg, *ACS Catal.*, 2021, **11**, 958–966.

31 J. Li, A. Ozden, M. Wan, Y. Hu, F. Li, Y. Wang, R. R. Zamani, D. Ren, Z. Wang, Y. Xu, D.-H. Nam, J. Wicks, B. Chen, X. Wang, M. Luo, M. Graetzel, F. Che, E. H. Sargent and D. Sinton, *Nat. Commun.*, 2021, **12**, 2808.

32 X. Fang, S. Wu, Y. Wu, W. Yang, Y. Li, J. He, P. Hong, M. Nie, C. Xie, Z. Wu, K. Zhang, L. Kong and J. Liu, *Appl. Surf. Sci.*, 2020, **518**, 146226.

33 D. Zeng, C. Li, W. Wang, L. Zhang, Y. Zhang, J. Wang, L. Zhang, X. Zhou and W. Wang, *Chem. Eng. J.*, 2023, **461**, 142133.

34 Y. Zhao, X. Zu, R. Chen, X. Li, Y. Jiang, Z. Wang, S. Wang, Y. Wu, Y. Sun and Y. Xie, *J. Am. Chem. Soc.*, 2022, **144**, 10446–10454.

35 W. Li, Z. Yin, Z. Gao, G. Wang, Z. Li, F. Wei, X. Wei, H. Peng, X. Hu, L. Xiao, J. Lu and L. Zhuang, *Nat. Energy*, 2022, **7**, 835–843.

36 C.-T. Dinh, T. Burdyny, M. G. Kibria, A. Seifitokaldani, C. M. Gabardo, F. P. G. de Arquer, A. Kiani, J. P. Edwards, P. D. Luna, O. S. Bushuyev, C. Zou, R. Quintero-Bermudez, Y. Pang, D. Sinton and E. H. Sargent, *Science*, 2018, **360**, 783–787.

37 R. Reske, H. Mistry, F. Behafarid, B. Roldan Cuenya and P. Strasser, *J. Am. Chem. Soc.*, 2014, **136**, 6978–6986.

38 H. Xiao, T. Cheng and W. A. Goddard III, *J. Am. Chem. Soc.*, 2017, **139**, 130–136.

39 Q. Fan, X. Zhang, X. Ge, L. Bai, D. He, Y. Qu, C. Kong, J. Bi, D. Ding, Y. Cao, X. Duan, J. Wang, J. Yang and Y. Wu, *Adv. Energy Mater.*, 2021, **11**, 2170140.

40 Y. Jiang, C. Choi, S. Hong, S. Chu, T.-S. Wu, Y.-L. Soo, L. Hao, Y. Jung and Z. Sun, *Cell Rep. Phy. Sci.*, 2021, **2**, 100356.

41 L. Xu, X. Ma, L. Wu, X. Tan, X. Song, Q. Zhu, C. Chen, Q. Qian, Z. Liu, X. Sun, S. Liu and B. Han, *Angew. Chem., Int. Ed.*, 2022, **61**, e202210375.

42 C. Chen, X. Yan, Y. Wu, S. Liu, X. Zhang, X. Sun, Q. Zhu, H. Wu and B. Han, *Angew. Chem., Int. Ed.*, 2022, **61**, e202202607.

43 X. Yan, C. Chen, Y. Wu, S. Liu, Y. Chen, R. Feng, J. Zhang and B. Han, *Chem. Sci.*, 2021, **12**, 6638–6645.

44 K. Yao, J. Li, H. Wang, R. Lu, X. Yang, M. Luo, N. Wang, Z. Wang, C. Liu, T. Jing, S. Chen, E. Cortes, S. A. Maier, S. Zhang, T. Li, Y. Yu, Y. Liu, X. Kang and H. Liang, *J. Am. Chem. Soc.*, 2022, **144**, 14005–14011.

45 X. Yuan, S. Chen, D. Cheng, L. Li, W. Zhu, D. Zhong, Z. J. Zhao, J. Li, T. Wang and J. Gong, *Angew. Chem., Int. Ed.*, 2021, **60**, 15344–15347.

46 P. Wang, H. Yang, C. Tang, Y. Wu, Y. Zheng, T. Cheng, K. Davey, X. Huang and S.-Z. Qiao, *Nat. Commun.*, 2022, **13**, 3754.

47 C.-T. Dinh, A. Jain, F. P. G. de Arquer, P. De Luna, J. Li, N. Wang, X. Zheng, J. Cai, B. Z. Gregory, O. Voznyy,

This journal is © The Royal Society of Chemistry 2024

J. Mater. Chem. A, 2024, **12**, 1218–1232 | **1231**

B. Zhang, M. Liu, D. Sinton, E. J. Crumlin and E. H. Sargent, *Nat. Energy*, 2019, **4**, 107–114.

48 S. Wang, D. Wang, B. Tian, X. Gao, L. Han, Y. Zhong, S. Song, Z. Wang, Y. Li, J. Gui, M. G. Sendeku, Y. Zhang, Y. Kuang and X. Sun, *Sci. China Mater.*, 2023, **66**, 1801–1809.

49 M. Zheng, P. Wang, X. Zhi, K. Yang, Y. Jiao, J. Duan, Y. Zheng and S.-Z. Qiao, *J. Am. Chem. Soc.*, 2022, **144**, 14936–14944.

50 H. Zhang, J. Gao, D. Raciti and A. S. Hall, *Nat. Catal.*, 2023, **6**, 807–817.

51 J. Feng, L. Zhang, S. Liu, L. Xu, X. Ma, X. Tan, L. Wu, Q. Qian, T. Wu, J. Zhang, X. Sun and B. Han, *Nat. Commun.*, 2023, **14**, 4615.